nuclear fusion
IAEA

PAPER • OPEN ACCESS

ELM penetration in ITB plasma on EAST tokamak

To cite this article: X. Gao *et al* 2025 *Nucl. Fusion* **65** 082001

OPEN ACCESS
IOP Publishing | International Atomic Energy Agency
Nuclear Fusion
Nucl. Fusion **65** (2025) 082001 (8pp)
https://doi.org/10.1088/1741-4326/adeac1

ELM penetration in ITB plasma on EAST tokamak

X. Gao[1], K.N. Geng[1,*], X.X. Zhang[1,*], K. Hanada[2], K.X. Ye[1], Y.F. Liang[3], Z. Zhou[1], L. Yu[1], G.S. Li[1], T. Zhang[1], Z.X. Liu[4], F.F. Long[4], G.Q. Li[1] and the EAST Team[1,a]

[1] Institute of Plasma Physics, Chinese Academy of Sciences, Hefei 230031, China
[2] Research Institute for Applied Mechanics, Kyushu University, Kasuga 816-8580, Japan
[3] Forschungszentrum Jülich GmbH, Institute für Energie-und Klimaforschung-Plasmaphysik, 52425 Jülich, Germany
[4] University of Science and Technology of China, Hefei 230026, China

E-mail: kngeng@ipp.ac.cn and xuexi.zhang@ipp.ac.cn

Received 16 December 2024, revised 4 June 2025
Accepted for publication 2 July 2025
Published 14 July 2025

Abstract

The penetration of an edge-localized mode (ELM) into an internal transport barrier (ITB) plasma has been studied on the EAST tokamak with a flat central safety factor profile $q(0) \sim 1$ recently. The experiment indicates that when the ELM inward penetration radius reaches the ITB foot region, a significant influence on the ITB plasma is manifested, leading to the shrinking or collapse of the ITB on the EAST tokamak. Observations suggest that the onset of large ELM penetration, which extremely reduces the pedestal temperature and density, can trigger the collapse of the ITB, by means of the off-axis sawtooth on the EAST tokamak. The off-axis sawtooth events contribute to a further decrement in the core stored energy after a larger ELM crash in the pedestal region. The reversal surface of the off-axis sawtooth is situated around the ITB foot. The delay time between the ELM penetration reached to the ITB foot and the followed off-axis sawtooth collapse is about 2–3 ms. It is also found that the expanding of ITB is related to the net heating power. Mechanism of ITB collapse from ELM penetration to the off-axis sawtooth triggered is not yet clear. Experimental results for understanding ELM penetration in ITB plasmas are summarized and discussed.

Keywords: ITB collapse, ELM, off-axis sawtooth, EAST tokamak

(Some figures may appear in colour only in the online journal)

[a] See Gong *et al* 2024 (https://doi.org/10.1088/1741-4326/ad4270) for the EAST Team.
[*] Authors to whom any correspondence should be addressed.

1. Introduction

Achieving high confinement performance is a paramount objective for future fusion reactors. Experimentally, this performance can be enhanced through the formation of transport barriers in both the plasma edge and core, known as the edge transport barrier (ETB) [1, 2] and the internal transport barrier (ITB) [3–6], respectively. Typically, the generation of a high fraction of non-inductive current is associated with the formation of a steep pressure gradient within the ITB region, and the fusion power is anticipated to scale with the square of the pedestal pressure in the ETB. Consequently, advanced operation scenarios featuring the coexistence of ETB and ITB have been explored extensively over the past two decades in various devices, including JET [7–10], JT-60U [11–13], TFTR [14, 15], Alcator C-Mod [16, 17], ASDEX-U [18–21], DIII-D [22–27], and EAST [28–31]. The interplay between ITB and ETB remains an unresolved issue due to the complex, self-organized interactions among them [32–34]. For instance, in JT-60U, the pedestal establishment during the L–H transition may be induced by a degradation of the ITB [35]. Conversely, the pedestal behavior can also influence the ITB dynamics, and the strength of the ITB has been observed to increase during the H-L transition in JT-60U. In the EAST tokamak, an electron ITB (e-ITB) is detected during the H-L transition, where the ITB foot moves inward until the L–H transition occurs, at which point the H-mode pedestal or type-I edge-localized modes (ELMs) significantly affect the e-ITB intensity [36]. Recent studies have investigated the impact of the pedestal or ELMs on ITB evolution. In JET, the collapse of the ITB induced by large-amplitude type I ELMs in ITB plasmas has been observed [37]. Electron cyclotron emission (ECE) data indicate that ITB contraction occurs as the ELM penetration radius reaches the ITB foot. Similarly, in JT-60U, when the ELM penetration radius extends to the ITB foot, the ITB width ceases to expand outward and ultimately reaches an equilibrium state [34].

These observations suggest that ELM penetration may be a critical factor in regulating ITB dynamics. Furthermore, this paper aims to investigate the influence of ELM penetration on ITB in two distinct scenarios on EAST tokamak, one involving the collapse of ITB and another where the ITB is sustained during ELMy H-mode without abrupt collapse. The structure of this paper is as follows: section 2 describes the experimental setup. Section 3 details the phenomena of ELM penetration and ITB collapse in hybrid plasma conditions. Section 4 presents the off-axis sawtooth observed during ITB collapse. Section 5 discusses the maintenance of a sustained ITB in ELMy H-mode without sudden collapse. Section 6 analyzes the impact of heating power on ITB movement and provides a summary of the findings and conclusions of this work.

2. Experimental setup

The experimental campaign was conducted on the EAST tokamak, a medium-sized superconducting tokamak characterized by a major radius of $R_0 = 1.85$ m and a minor radius $a =$ 0.45 m. The EAST device is equipped with a molybdenum wall in the main chamber, a graphite bottom divertor, and an ITER-like tungsten/copper (W/Cu) top divertor. The plasma current (I_p) of 450 kA is counter-clockwise in the view of the top, while a toroidal magnetic field (B_T) of 1.6 T is applied in the clockwise direction. The experiments were carried out in hybrid H-mode discharges with low hybrid wave (LHW) heating at 4.6 GHz and neutral beam injection (NBI) with a lower single null divertor configuration. As shown in figure 1(*a*), the NBI system has two beams (each consisting of two ion sources), one is co-tangential (NBI1) and the other is counter-tangential (NBI2), they can provide toroidal momentum injection along/against the direction of the plasma current respectively [38].

The poloidal arrangement of the diagnostics used in this work is in this study illustrated in figure 1(*b*). An 11-channel POLarimeter-INTerferometer (POINT) was utilized to measure the line-averaged density across 11 horizontal chords, with an adjacent vertical spacing of 8.5 cm [39–41]. The ECE channels located at mid-plane on the low field side are utilized for the measurement of electron temperature. The soft X-ray (SXR) diagnostic provides information on MHD properties such as sawtooth instability in this work.

3. ELM penetration and ITB collapse in the hybrid plasma

Figure 2 presents the waveform of a typical H-mode discharge. As shown in figure 2(*a*), the plasma current ramps up to 450 kA at 2.2 s. The 4.6 GHz LHW power (1 MW) works as a preheating power throughout the flattop phase. The NBI heating increases stepwise with about 1.1 MW in the first two NBI1 sources and 0.9 MW in the latter two NBI2 sources, respectively. The L–H transition is initiated at $t = 2.45$ s with the input of the first NBI source, followed by the emergence of ELM spikes approximately 0.1 s later, as observed in the D_α emission (see figure 2(*f*)). As shown in figures 2(*c*)–(*e*), when the last NBI source is injected into the plasma, the stored energy increases from 140 to 190 kJ, which is much higher than the increment of stored energy caused by the second and third sources. Meanwhile, the $H_{98,y2}$ factor increases from 1 to 1.1 with a decreased internal inductance (li), which suggests an improvement of confinement from the standard ELMy H-mode. The difference between core and edge density shows a continuous increase during this period, which indicates the formation of an n_e-ITB. The formation of the ITB in T_e, and T_i is also found during this period, the details of which can be found in [28]. As shown in figure 2(*c*), the start time of ITB formation is identified at $t = 3.59$ s with a black dashed line. Approximately 0.2 s subsequent to this, a sudden collapse of the ITB occurs, concomitant with a decrease in stored energy, the $H_{98,y2}$ factor, and core density.

Figure 3 shows the evolution of the stored energy, D_α emission, as well as the ELM penetration radius and the location of the ITB-foot for the period presented by the blue rectangle in figure 2. Here, the penetration radius of ELM in figure 3(*c*) is evaluated by the drop of the electron temperature within

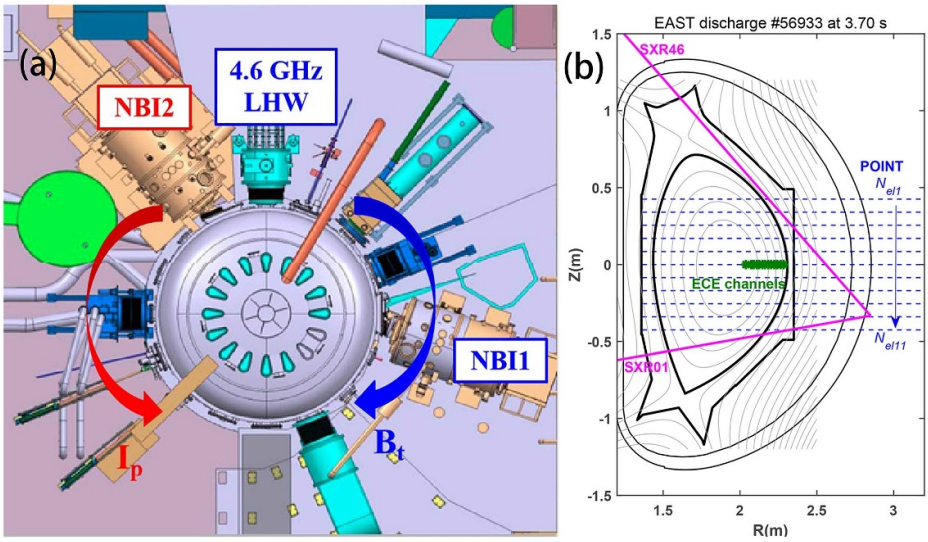

Figure 1. (*a*) Toroidal and (*b*) poloidal arrangements of the heating and diagnostics, where SXR01-SXR46 (pink line) is the channel 1–46 of soft x-ray, and N_{el1}–N_{el11} (blue dashed line) correspond to channel 1 to channel 11 of POINT, green stars denote the ECE channels.

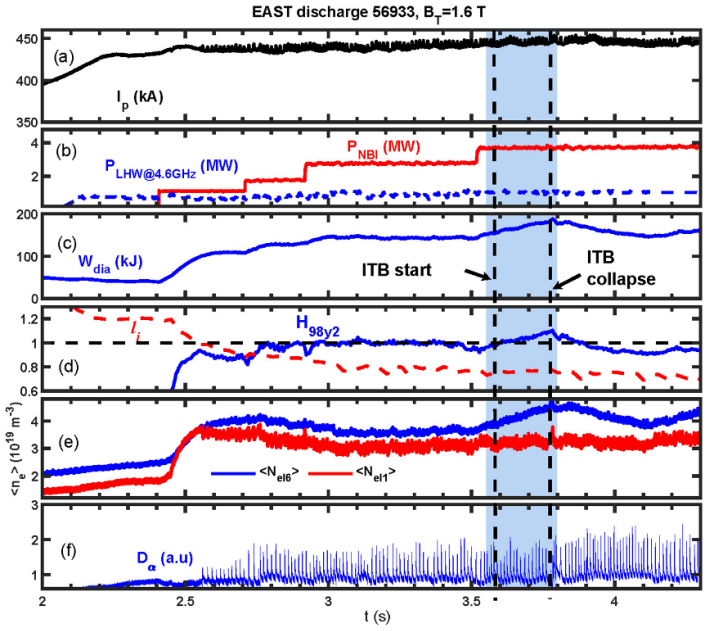

Figure 2. Evolution of basic parameters in a typical discharge: (*a*) plasma current I_p, (*b*) 4.6 GHz LHW power and NBI power, (*c*) diamagnetic stored energy W_{dia}, (*d*) internal inductance (*li*) and $H_{98,y2}$ factor, where $H_{98,y2}$ is the thermal energy confinement time normalized to a scaling relation, (*e*) line-averaged electron density from channel 1 and 6 of POINT, (*f*) D_α emission. The dashed lines indicate the ITB start and collapse time, while the blue rectangle shadow indicates time interval used in figure 3.

600 μs after the ELM crash, i.e. the radius is defined as the deepest radial location with $\Delta Te/Te > 1\%$ as referenced in [34]. The ECE data is firstly filtered with a 2 kHz low-pass filter to avoid the effect of high frequency perturbation on the measurement of temperature. Then, the changes in temperature caused by ELMs are calculated by this definition. Considering the distance between the ECE channels, the penetration depth is calculated by fitting the temperature changes of these channels. The radius of ITB-foot expands outward with the increase of stored energy, while the penetration radius does not show a clear trend in the early phase before 3.72 s. However, as the ITB foot gradually expands outward, the penetration radius of ELM tends to deepen inward from 3.73 s. In special, it is seen at $t = 3.78$ s, when ELM penetration radius reaches to ITB foot at around $\rho \sim 0.44$, ITB starts to collapse as shown in figure 3(*a*). During the collapse, the stored energy decreases from 190 kJ to 167 kJ. In the next section, the evolution of ITB collapse will be shown.

In fact, the ITB collapse caused by the ELM penetration is not a random event, and the same phenomenon can be seen in other shots. Here, the statistical result of the ELM crash and ITB collapse of the shot in #56932 and #56933 are shown in

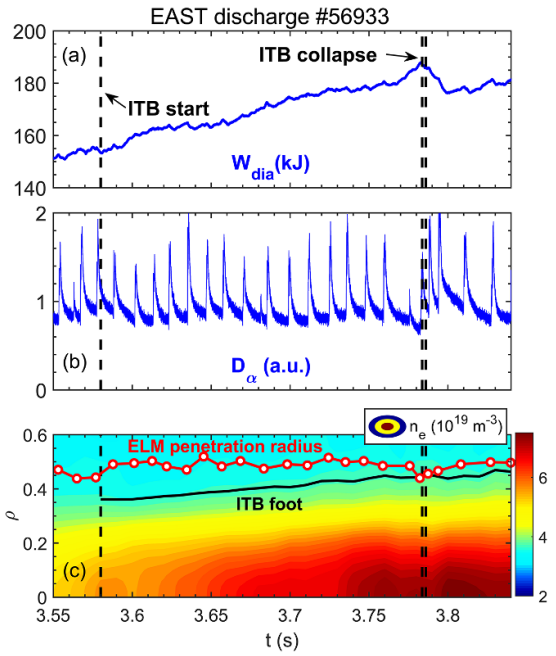

Figure 3. (*a*) Stored energy, (*b*) D_α emission, (*c*) contour of electron density, the location of pressure ITB foot (black solid line) as well as ELM penetration radius (red circle line). The penetration depth is defined from the ECE data, the density contour figure and the location of ITB foot are calculated by the density profile measured by the POINT diagnostic, which is calibrated by the Thomson scattering (TS) laser diagnostic.

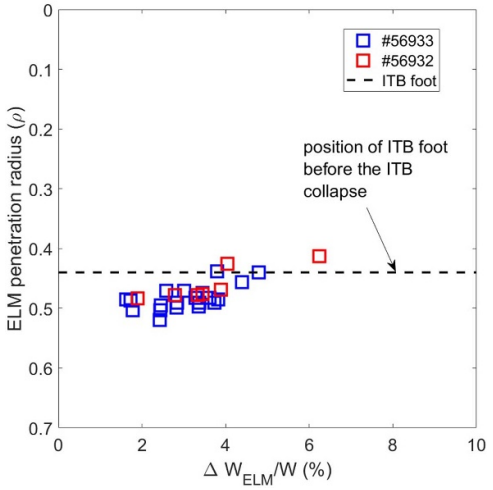

Figure 4. Statistics of ELM size and penetration depth.

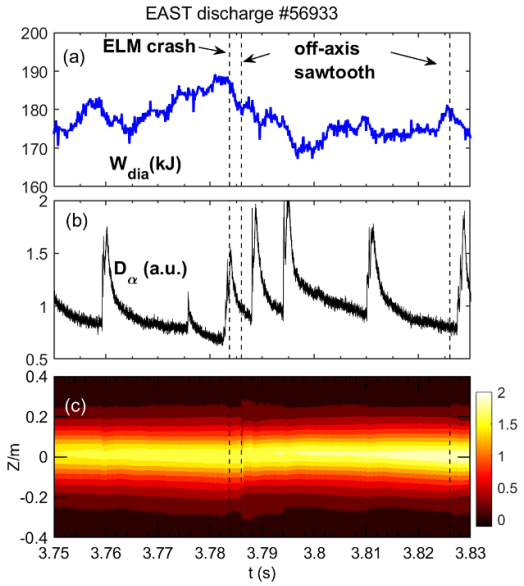

Figure 5. (*a*) Stored energy, (*b*) D_α emission, (*c*) SXR radiation distribution. The collapse time and off-axis sawteeth (ST) are indicated by vertical dashed lines.

figure 4. Here, the $\Delta W_{\mathrm{ELM}}/W$ is calculated using stored energy to represent the size of the ELM crash, the penetration radius of the ELM is calculated as described, and the position of the ITB foot before the ITB collapse is shown in dashed lines in figure 4. In shot #56932, the discharge parameters are the same as shot #56933 in the manuscript, the location of the ITB foot is similar to #56933 around $\rho \sim 0.44$ before ITB collapse. It is shown that in the blue and red rectangles in figure 4, when the ELM size is large, the depth of ELM penetration can increase with ELM size. This result is similar with JT-60U [34], in which the penetration radius of T_{e}, T_{i} and V_{t} increases with the ELM size. This result indicates that the ITB collapse is correlated with the amplitude of the ELM size and penetration depth.

4. Off-axis sawtooth observed during ITB collapse

Figure 5 shows the evolution of stored energy, D_α emission, as well as the distribution of SXR radiation. It is shown that the ITB collapse starts with an ELM burst at approximately 3.783 s. Subsequently, during the collapse, an off-axis sawtooth is triggered at $t = 3.786$ s within the core plasma, with the reversal surface at approximately $Z = 0.25$ m, which corresponds to a normalized radius of $\rho = 0.44$. When the sawtooth is triggered, the stored energy further decreases. Such off-axis sawtooth is also found at 3.826 s when the stored energy decreases. It is noted that the reversal surface of off-axis sawtooth is quite different from the regular one, the reversal surface of off-axis sawtooth is around $\rho = 0.44$ while the reversal surface of regular sawtooth is around $\rho = 0.3$ at $q = 1$ surface in this shot, as shown in [28].

During the ITB collapse, an $n = 1$ precursor is often observed in the spectrogram of the SXR signal. Figure 6 shows the evolution of the raw core SXR signal and its spectrogram. Figure 6(*d*) shows the amplitude of the precursor with [4 6] kHz filter and its envelope. As shown in figures 6(*c*) and (*d*), a 4 kHz precursor is observed after the ELM crash, and the amplitude of the precursor gradually increases and then decreases before the onset of the next ELM.

ECE is also employed to examine the spatial dynamics of the sawtooth behavior. Figures 7(*a*)–(*j*) present the temporal evolution of the electron temperature at different normalized

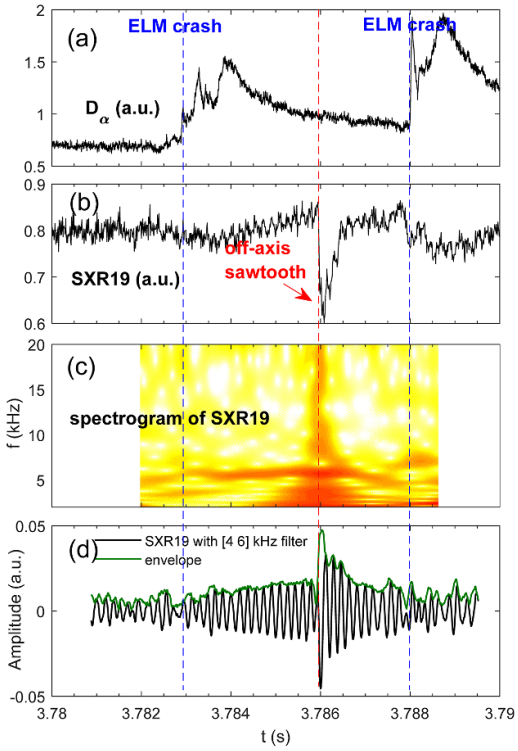

Figure 6. (*a*) D_α emission, (*b*) channel 19 of SXR (SXR19) radiation at core, (*c*) spectrogram of SXR19, (*d*) amplitude of SXR19 with [4 6] kHz filter and its envelope.

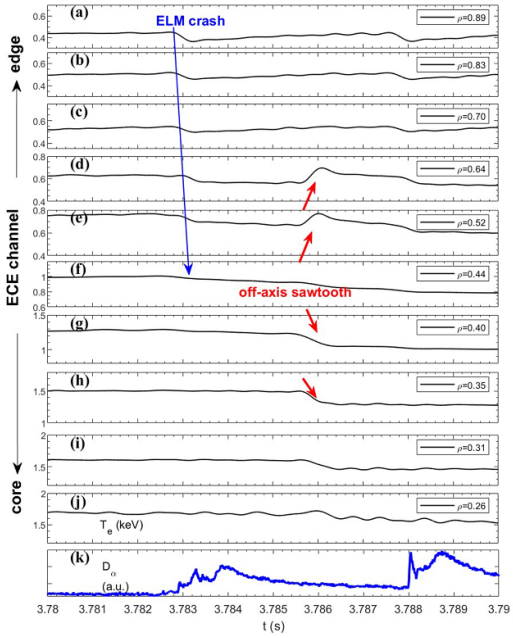

Figure 7. (*a*)–(*j*) Evolution of electron temperature measured by different ECE channels from edge to core with 2 kHz low-pass filter. Blue arrow shows the influence of the ELM penetration from edge to the core. Red arrows show the further collapse in shot #56933. (*k*) D_α emission.

radius from the edge to the core plasma. The blue arrow in these figures points to a significant drop in the edge temperature, which is correlated with the occurrence of an ELM crash as shown in figure 7(*k*). This rapid decrease in temperature could even extend to a radial position of $\rho = 0.44$. Such *a* T_e change in different positions causes an increase of *the* T_e gradient in the ITB region after the ELM crash, which could trigger the 5 kHz precursor and lead to the occurrence of off-axis sawtooth at $t = 3.786$ s. It is noticed that the reversal of the surface of off-axis sawtooth just corresponds to the depth of ELM penetration in $\rho = 0.44$, which is also the location of ITB foot. This implies that when the ELM penetration reaches the region of the ITB foot, it induces a substantial alteration in the local gradient or the q profile, thereby triggering an off-axis sawtooth instability that eventuates in the collapse of the ITB.

5. Sustained ITB in ELMy H-mode without collapse

As a comparison, a sustained ITB plasma in ELMy H-mode (#71320) without an abrupt collapse is shown in figure 8. The plasma enters H-mode with 1.2 MW NBI and 1 MW LHW power. After the input of the second NBI source ($t = 3$ s), a $m/n = 1/1$ fishbone instability is triggered, as shown in figure 8(*e*). The ITB starts from $t = 3.53$ s and is closely related to the triggering of the fishbone. The gradient of the electron density in the ITB region increases with the burst of fishbone instability [30]. In our previous study [29], energy transport analysis has shown that the fishbone instabilities have a suppression on electron turbulent energy transport. From $t = 3.53$ s, the high normalized beta (β_N) plasma with ETB and ITB is maintained for about 3 s. In the flattop ($t = 4$–6 s) with NBI power of 4.8 MW and LHW power of 1.2 MW, the β_N achieves a maximum value of 1.9 and is sustained for 2 s. Figures 8(*f*)–(*h*) show the profiles of electron density, electron temperature and ion temperatures at 4.5 s and 6 s, respectively. As shown in the figure, the ITB foot locates at $\rho = 0.3$, which is also the position where the fishbone instability is triggered. In shot #71320, the ITB remains in a quasi-steady state until the termination of the NBI.

The evolution of the stored energy, D_α emission, as well as the ELM penetration radius and the location of the ITB-foot during 4.5–5 s (#71320) are presented in figure 9. In this quasi-steady state, the ELM penetration radius does not reach the ITB foot, and the ITB foot and stored energy are hardly affected. As a result, both the ITB and ETB can be sustained for steady state on the EAST tokamak as shown in figure 9(*d*).

6. Discussion and summary

In this report, the ELM penetrations in different ITB discharges are discussed, and the results show that the depth of penetration is a crucial issue in the maintenance of ITB. In addition to the ELM penetration, the movement of ITB is also important for maintaining ITB. In JET, the transition from type-III to large type-I ELM often causes a deeper penetration reaching to the ITB foot and causing the ITB foot to shrink inward [37]. This phenomenon could be related to the insufficient injected power. Here, the power crossing the separatrix

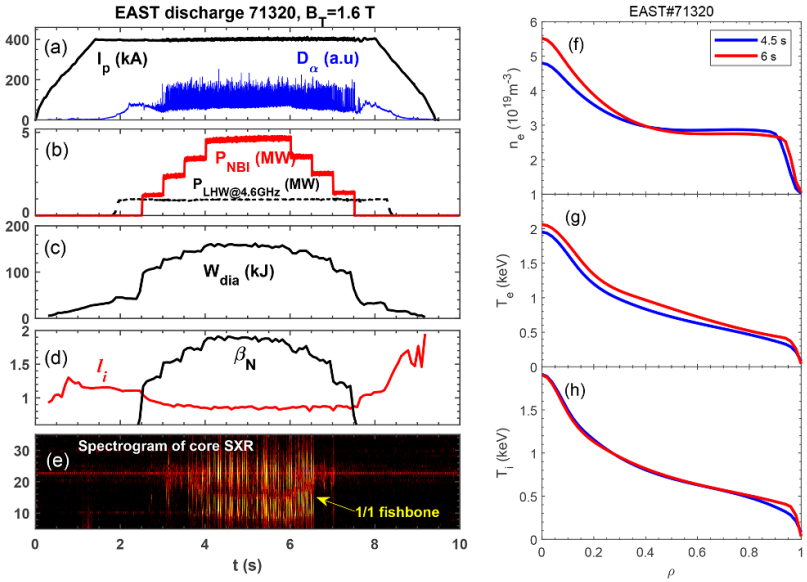

Figure 8. Quasi-steady state high β_N discharge (#71320) with ITB on EAST. (*a*) Plasma current I_p and the D_α emission signal. (*b*) 4.6 GHz LHW power and NBI power, (*c*) diamagnetic stored energy W_{dia}, (*d*) internal inductance *li* and plasma normalized beta β_N and (*e*) spectrogram of core SXR showing the $m/n = 1/1$ fishbone instability. (*f*)–(*h*) Electron density, electron temperature and ion temperature profiles for H-mode with ITB phase at $t = 4.5$ s (blue) and 6 s (red).

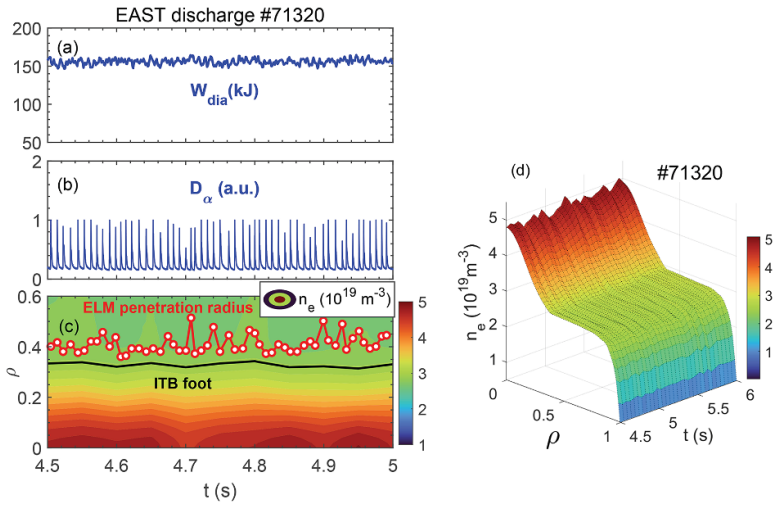

Figure 9. (*a*) Stored energy, (*b*) D_α emission, (*c*) contour of electron density, the location of pressure ITB foot (black solid line) as well as ELM penetration radius (red circle line). (*d*) Evolution of n_e profile.

is defined as $P_{sep} = P_{in} - dW/dt - P_{rad}$, the three items on the right hand side are the injected power, time derivative of the plasma diamagnetic energy and radiation power, respectively. In their experiment, the first large type-I ELM occurred during the slowing down of the ICRF power; this large ELM leads to an increase in the radiation power and a reduction of the power crossing the separatrix for entering type-III H-mode. As a result, the ITB foot performs a continuous shrinking when the penetration radius of type-I ELM reaches the ITB foot. On the contrary, in JT-60U it is found that when the additional negative ion source NB power is turned on, the ITB foot is expanding till the type I ELM penetration reaches to the ITB foot, finally, it comes to a balance state [33].

In early experiments on EAST, the radiation power is often underestimated because of the incomplete coverage of viewing chords on the divertor region and strong low-charge emission in the edge plasma. Here, we replace the P_{sep} with the loss power ($P_{loss} = P_{in} - dW/dt$). As depicted in figure 10, during the EAST experiment (shot #56933), the injected power remains nearly constant during 3.55–4 s, while the stored energy initially rises ($dW/dt > 0$) before subsequently declining ($dW/dt < 0$). The ITB expands until the ELM penetration reaches the ITB foot, at which point the ITB begins to collapse at $t = 3.77$ s. The ITB foot maintains a transient balance state from 3.77 to 3.85 s, after which it starts to shrink inward at $t = 3.85$ s. This expansion of the ITB appears to be correlated

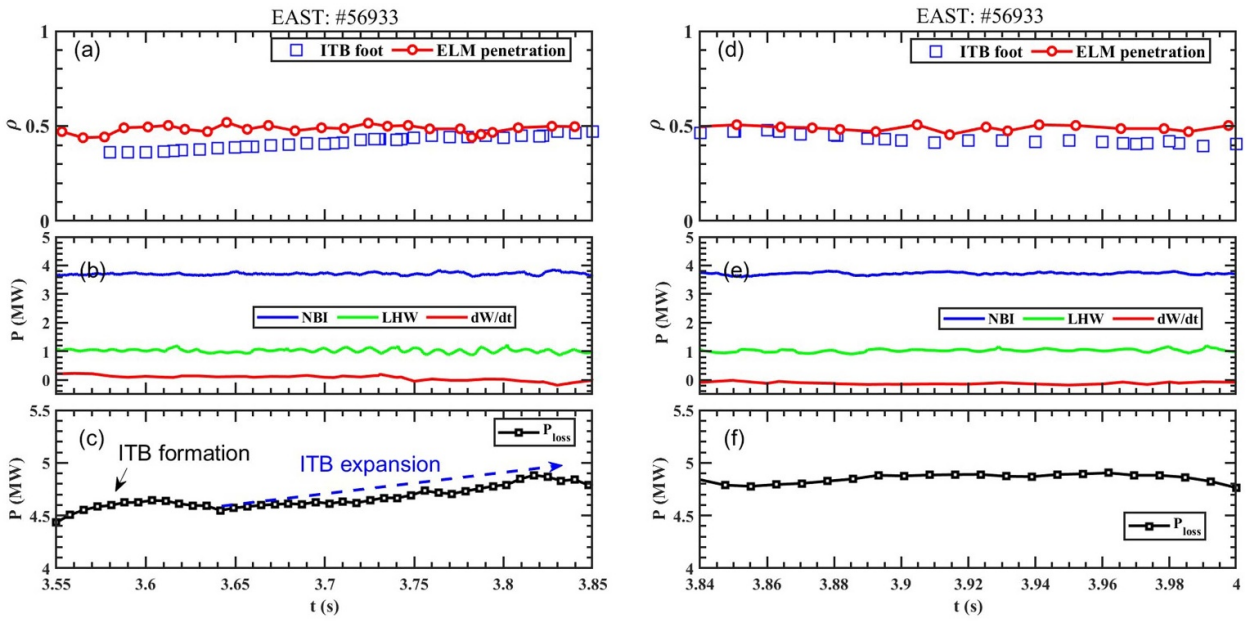

Figure 10. Evolution of (*a*) and (*d*): ITB foot and ELM penetration, (*b*) and (*e*): injected power and time derivative (dW/dt) of stored energy, (*c*) and (*f*): loss power $P_{\rm loss}$.

with the trend observed in the loss power ($P_{\rm loss}$). This dependence on power is similar to results in JT-60U. However, in the ITB shrinking phase, where $P_{\rm loss}$ remains constant, no clear correlation is found between ITB shrinking and net heating power variation.

In summary, the ELM penetration and ITB collapse has been studied in the EAST tokamak. When the ELM penetration radius reaches the ITB foot, a significant impact on the ITB plasma is observed as the ITB shrinks or collapses. However, when the ELM penetration radius does not reach the ITB foot, both ITB and ETB plasmas can be sustained steadily with type-I ELM. When the ITB collapse starts, the off-axis sawtooth happens to decrease the stored energy further. The reversal surface of the off-axis sawtooth is around the ITB foot. The delay time between the ELM penetration reach to the ITB foot and the off-axis sawtooth collapse is about 2–3 ms. The mechanism of ITB collapse from ELM penetration to the off-axis sawtooth triggered is not yet clear. It is also found that the expanding of ITB is correlated with the net heating power. Further studies in simulation are needed, and a boundary and pedestal integration module for the BOUT++ code is under development.

Acknowledgments

This work has been supported by the National Key R&D Program of China (Contract Nos. 2022YFE03050003, 2019YFE03040004, 2022YFE03020004, 2019YFE03080200, and 2022YFE03070004) and the National Nature Science Foundation of China (Grant Nos. 12175277, 12405271 and 12275315). This work was supported by the Open Fund of Magnetic Confinement Laboratory of Anhui Province (No. 2023AMF03005), and the Science Foundation of Institute of Plasma Physics, Chinese Academy of Sciences (No. DSJJ-2024-08), as well as the President Funding of Hefei Institutes of Physical Science, Chinese Academy of Sciences (No. YZJJ2024QN22). This work was supported by the RIAM joint usage/research project in 2024. We thank the staff members at EAST (https://cstr.cn/31130.02.EAST), for providing technical support and assistance in data collection and analysis.

References

[1] Wagner F. *et al* 1982 *Phys. Rev. Lett.* **49** 1408
[2] Itoh S.I. and Itoh K. 1988 *Phys. Rev. Lett.* **60** 2276
[3] Koide Y. *et al* 1994 *Phys. Rev. Lett.* **72** 3662
[4] Doyle E. *et al* 2007 *Nucl. Fusion* **47** S18
[5] Shimada M. *et al* 2007 *Nucl. Fusion* **47** S1
[6] Gormezano C. *et al* 2007 *Nucl. Fusion* **47** S285
[7] Tresset G., Litaudon X., Moreau D. and Garbet X. (Contributors to the EFDA-JET Work Programme) 2002 *Nucl. Fusion* **42** 520
[8] Joffrin E. *et al* 2002 *Plasma Phys. Control. Fusion* **44** 1739
[9] Joffrin E. *et al* 2003 *Nucl. Fusion* **43** 1167
[10] Conway G.D., Borba D.N., Alper B., Bartlett D.V., Gormezano C., von Hellermann M.G., Maas A.C., Parail V.V., Smeulders P. and Zastrow K.-D. 2000 *Phys. Rev. Lett.* **84** 1463
[11] Oyama N. *et al* 2009 *Nucl. Fusion* **49** 104007
[12] Sakamoto Y. *et al* 2001 *Nucl. Fusion* **41** 865
[13] Nazikian R. *et al* 2005 *Phys. Rev. Lett.* **94** 135002
[14] Mazzucato E. *et al* 1996 *Phys. Rev. Lett.* **77** 3145
[15] Bell M.G. *et al* 1999 *Plasma Phys. Control. Fusion* **41** A719
[16] Fiore C.L. *et al* 2012 *Phys. Plasmas* **19** 056113
[17] Fiore C.L. *et al* 2001 *Phys. Plasmas* **8** 2023–8
[18] Günter S. *et al* 2000 *Phys. Rev. Lett.* **84** 3097
[19] Quigley E.D., Peeters A.G., Carthy P.J.M., Apostoliceanu M., Hobirk J., Igochine V. and Meister H. (the ASDEX Upgrade Team) 2004 *Nucl. Fusion* **44** 1189

[20] Conway G.D. *et al* 2001 *Plasma Phys. Control. Fusion* **43** 1239
[21] Joffrin E. *et al* 2002 *Plasma Phys. Control. Fusion* **44** 1203
[22] Greenfield C.M. *et al* 2000 *Phys. Plasmas* **7** 1959–67
[23] Garofalo A.M. *et al* 2015 *Nucl. Fusion* **55** 123025
[24] Austin M.E. *et al* 2006 *Phys. Plasmas* **13** 082502
[25] Shafer M.W., McKee G.R., Austin M.E., Burrell K.H., Fonck R.J. and Schlossberg D.J. 2009 *Phys. Rev. Lett.* **103** 075004
[26] Rettig C.L., Burrell K.H., Stallard B.W., McKee G.R., Staebler G.M., Rhodes T.L., Greenfield C.M. and Peebles W.A. 1998 *Phys. Plasmas* **5** 1727–35
[27] Doyle E.J. *et al* 2000 *Plasma Phys. Control. Fusion* **42** A237
[28] Yang Y. *et al* 2017 *Plasma Phys. Control. Fusion* **59** 085003
[29] Gao X. *et al* 2020 *Nucl. Fusion* **60** 102001
[30] Gao X. *et al* 2018 *Phys. Lett. A* **382** 1242–6
[31] Wu M.F. *et al* 2023 *Nucl. Fusion* **63** 016008
[32] Kamada Y., Takenaga H., Isayama A., Hatae T., Urano H., Kubo H., Takizuka T. and Miura Y. 2002 *Plasma Phys. Control. Fusion* **44** A279
[33] Kamada Y., Oyama N., Ide S., Sakamoto Y., Isayama A., Fujita T., Urano H., Suzuki T. and Yoshida M. 2006 *Plasma Phys. Control. Fusion* **48** A419
[34] Kamada Y., Yoshida M., Sakamoto Y., Koide Y., Oyama N., Urano H., Kamiya K., Suzuki T. and Isayama A. 2009 *Nucl. Fusion* **49** 095014
[35] Neudatchin S.V., Takizuka T., Shirai H., Fujita T., Isayama A., Kamada Y., Koide Y., Suzuki T. and Takeji S. 2002 *Plasma Phys. Control. Fusion* **44** A38
[36] Han X. *et al* 2022 *Nucl. Fusion* **62** 064005
[37] Sarazin Y. *et al* 2002 *Plasma Phys. Control. Fusion* **44** 2445
[38] Geng K.N. *et al* 2021 *Nucl. Fusion* **61** 056011
[39] Liu H.Q. *et al* 2014 *Rev. Sci. Instrum.* **85** 11D405
[40] Zou Z.Y. *et al* 2014 *Rev. Sci. Instrum.* **85** 11D409
[41] Zhu X., Zeng L., Liu H., Jie Y., Zhang S., Hu J. and Gao X. 2015 *Plasma Sci. Technol.* **17** 733